Eur. Phys. J. Spec. Top.
https://doi.org/10.1140/epjs/s11734-025-02112-x

THE EUROPEAN PHYSICAL JOURNAL SPECIAL TOPICS

Regular Article

Data-driven identification of macroscopic dynamics with implicit equation-free sampling and Gaussian process regression: for the example of an integrate-and-fire neural network

Torben Settmacher[1], Hannes Wallner[1], Konstantinos Spiliotis[2], Constantinos Siettos[3], and Jens Starke[1,a]

[1] Institute of Mathematics, University of Rostock, Rostock, Germany
[2] Laboratory of Mathematics and Informatics (ISCE), Department of Civil Engineering, Democritus University of Thrace, Xanthi, Greece
[3] Dipartimento di Matematica e Applicazioni "Renato Caccioppoli", Università degli Studi di Napoli Federico II, Naples, Italy

Received 30 September 2025 / Accepted 16 December 2025

Abstract We investigate a data-driven approach to derive low-dimensional macroscopic models of complex systems with only high-dimensional microscopic descriptions available. This is achieved by sampling of the macroscopic behaviour at selected points using an implicit equation-free approach with appropriate initialisation of the microscopic system. This enables subsequent data-driven identification of the macroscopic dynamics with Gaussian process regression. We demonstrate the technique on a high-dimensional neural network of integrate-and-fire neurons. A numerical bifurcation analysis of the obtained macroscopic model is performed, showing both stable and unstable branches. The appropriate sampling using the implicit equation-free approach avoids grid distortion and prevents spurious states as well as other artefacts.

1 Introduction

Many important real-world phenomena appear in complex systems which are modelled by high-dimensional systems of differential equations. Such systems can typically be described by a detailed microscopic model with a large number of states and equations. Nevertheless, they often exhibit macroscopic behaviour at a coarser level of description. In some cases, it is possible to approximate analytically this macroscopic behaviour. As a representative example, H. Haken and R. Graham derived a macroscopic description of the laser [1], successfully generalised this approach to other applications and established the field of synergetics; see, e.g. Refs. [2, 3]. Based on this work, similar methods were applied in the field of neuroscience [4–10], where thousands of neurons are coupled and define a high-dimensional microscopic model and low-dimensional macroscopic behaviour emerges as action and cognition [11]. Central in this and related methods is the approximation of the dynamic behaviour on the low-dimensional attractive slow invariant manifold [12] for constructing the macroscopic dynamics, i.e. reduced-order models [13–25].

Over the last few years, scientific machine learning has been used to solve inverse problems, where macroscopic models are learned in the form of black-box surrogate ODEs or PDEs [26–34] or in the form of *graybox*-physics-informed SDEs, ODEs and PDEs [25, 35–42] from data and simulations at the microscopic level. For a review, see also Refs. [32, 40, 43–45]. In recent years, there has been a large body of work applying machine learning to neuroscience, which roughly falls into two complementary directions (for a review, see also Ref. [46]). The first

T. Settmacher and H. Wallner have contributed equally to this work.

In memory of Hermann Haken.

[a] e-mail: jens.starke@uni-rostock.de (corresponding author)

Published online: 12 January 2026

approach learns surrogate models directly from spatio-temporal neural data (e.g. fMRI spatio-temporal recordings or other neuroimaging techniques) [47–52]. For example, neural networks and Gaussian processes have been used to build data-driven models in latent spaces with the aid of manifold learning [53, 54]. The second direction uses detailed mechanistic neurobiological simulations ranging from single-neuron biophysical models (such as Hodgkin–Huxley–type, and integrate-and-fire models) to mesoscopic neural-mass or mean-field models (e.g. the Wilson–Cowan and the FitzHugh–Nagumo PDEs) [32, 55, 56] and large-scale connectome-based whole-brain simulators [57–59] to construct reduced-order models.

In the present work, we mainly focus on the second direction, to construct surrogate reduced-order models, i.e. models of the macroscopic behaviour of complex systems with Gaussian process regression (GPR) by appropriate data sets from detailed simulations of a high-dimensional network of integrate-and-fire neurons [60–62]. Based on this, the aim is to use the obtained macroscopic models for a bifurcation and stability analysis of the macroscopic dynamics. Overall, we bridge microscopic detailed neuronal simulators with macroscopic level analysis tasks with a combination of an implicit equation-free approach and Gaussian process regression.

Equation-free analysis is a numerical method enabling the analysis of macroscopic behaviour from short microscopic simulations [63, 64] without an explicitly given macroscopic description. Coupling short microscopic simulations with fine graining yields a coarse time-stepper for macroscopic evolution without analytically deriving macroscopic equations. The described situation of microscopic and macroscopic scales is also characteristic in the field of neuroscience, where the equation-free approaches helps in the macroscopic analysis of neural models [46, 65–68]. While in the equation-free approach numerical analysis of the macroscopic behaviour can be performed locally, no global macroscopic model can be obtained. In the following, we use Gaussian process regression [69] to construct a global macroscopic differential equation from data, representing the relevant region of the phase space, with a number of local macroscopic right-hand sides. In order to obtain data at the required points in the macroscopic phase space, the implicit equation-free approach [70–72] is utilised.

In recent years, alternative ideas of bridging the equation-free framework with manifold learning and machine learning have been proposed for the development of the so-called *next generation* equation-free algorithms towards the construction of low-dimensional surrogate *global* models that can be used for a bifurcation analysis but also for gaining physical insight. For details, see Refs. [25, 30, 32, 39, 40, 54, 73–75].

The combination of equation-free modelling together with Gaussian process regression provides a probabilistic model for the macroscopic right-hand side. Gaussian process regression in the context of non-parametric ODE modelling has for example been investigated in Ref. [76]. The macroscopic model allows evaluations at out-of-sample points, offering global information for the considered region of the phase space and can be used for a variety of tasks on the macroscopic scale. Unlike other approaches, in this non-parametric approach, one can infer a model directly from noisy data, without having to choose so-called library or candidate functions required by other data-driven approaches, such as Sparse Identification of Nonlinear Dynamics (SINDy) [36], resulting in high flexibility and even uncertainty estimations. Recent studies utilise Gaussian process regression for the detection of bifurcation points [77].

This paper is organised as follows. In Sect. 2, we first give a brief overview of equation-free modelling followed by a detailed description of the data acquisition process and a short introduction into Gaussian process regression. In Sect. 3, we study a high-dimensional neural system of integrate-and-fire neurons and apply our approach to describe the macroscopic network dynamics followed by an investigation of the long-time behaviour in form of a bifurcation analysis of the macroscopic stationary states. We compare our findings to the results of a quasi-stationary up and down sweep as well as a equation-free pseudo-arclength continuation. The paper is concluded with a discussion.

2 System identification of the macroscopic dynamics with data-driven methods

In order to obtain a macroscopic vector field, i.e. the right-hand side of a macroscopic differential equation for selected points in the phase space of macroscopic behaviour, with only microscopic equations at hand, the equation-free approach is briefly summarised in Sect. 2.1. When sampling points in the phase space, there exist two distinct methods of equation-free analysis, namely an explicit and implicit approach, which are discussed in detail in Sects. 2.2 and 2.3. To acquire a global representation of the macroscopic model, this locally pointwise obtained vector field $F(\xi)$ at positions ξ can be used for Gaussian process regression, enabling out-of-sample evaluations of the macroscopic model $F(x)$ with $x \neq \xi$, which is discussed in Sect. 2.4.

2.1 Implicit equation-free analysis

Typically, high-dimensional complex systems exhibit a low-dimensional macroscopic behaviour. For these complex systems, microscopic models are available, which are described by large systems of differential equations. However, we are usually interested in the macroscopic behaviour for which no explicit model equations are known. I.

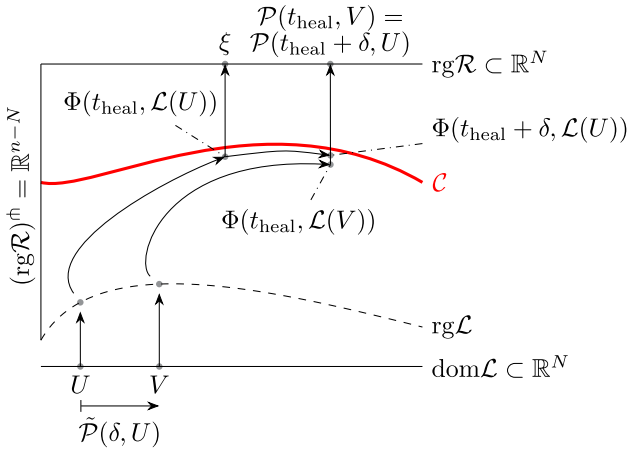

Fig. 1 Graphical illustration of the implicit equation-free approach. In the equation-free method, we map the macroscopic state U to the microscopic scale via the lifting operator $\mathcal{L} : \text{dom}\mathcal{L} \to \text{rg}\mathcal{L}$ with the domain $\text{dom}\mathcal{L}$ and range $\text{rg}\mathcal{L}$. The acquired microscopic state now evolves in the arbitrarily chosen transversal component $\text{rg}\mathcal{R}^{\pitchfork}$ towards the attractive slow manifold $\mathcal{C}$. After evolution of the microscopic system, the restriction operator $\mathcal{R} : \text{dom}\mathcal{R} \to \text{rg}\mathcal{R}$ can be used to map back to the macroscopic scale. The unknown macroscopic state V is defined implicitly by equation (1). The macroscopic state ξ marks the healed state $\mathcal{P}(t_{\text{heal}}, U) = \mathcal{R}(\Phi(t_{\text{heal}}, \mathcal{L}(U)))$. For sampling the data on given positions, e.g. a regular grid, for a given macroscopic value ξ, the initial state U is obtained implicitly by Eq. (3). The macroscopic time derivative is approximated by the difference quotient between the healed states $\mathcal{R}(\Phi(t_{\text{heal}} + \delta, \mathcal{L}(U)))$ and ξ. When solving the implicit equation iteratively, the condition $\text{rg}\mathcal{R} \subseteq \text{dom}\mathcal{L}$ has to hold. Adapted after [70–72]

Kevrekidis et al. [63, 64] introduced the so-called explicit equation-free analysis, which enables to explore the macroscopic behaviour of systems by performing short simulations of the high (n-)dimensional system of differential equations. The central assumption of this approach is the existence of a lower dimensional description of the systems dynamics via the ordinary differential equation $\dot{U} = F(U)$ for a few macroscopic states $U \in \mathbb{R}^N$ with $N \ll n$. Geometrically, we assume that the trajectories of the given high (n-)dimensional system converge quickly to a low-dimensional slow manifold $\mathcal{C}$; see also Fig. 1. Thus, the long-term dynamics described by the macroscopic states evolve on the slow manifold while the remaining states become enslaved [2, 3] to the slow dynamics.

Mapping between the scales is enabled through a so-called lifting operator (macro to micro) $\mathcal{L} : \mathbb{R}^N \to \mathbb{R}^n$ and a so-called restriction operator (micro to macro) $\mathcal{R} : \mathbb{R}^n \to \mathbb{R}^N$. Choosing a good restriction operator and macroscopic state, usually requires expert knowledge, especially in real-world applications. Recent efforts tried to construct automated lifting and restriction operators directly from data [73, 78]. The evolution of the system on the microscopic scale is carried out by the microscopic time-stepper Φ, which maps the micro-states to their time-δ image, i.e. $u(t+\delta) = \Phi(\delta, u(t))$. Thus, given an initial macroscopic state U, we are able to access the macroscopic state at time δ with $P(\delta, U) : U \mapsto V$ by the lift–evolve–restrict scheme

$$V = \mathcal{P}(\delta, U) = \mathcal{R}(\Phi(\delta, \mathcal{L}(U))).$$

When using this explicit scheme, a lifting operator is required which maps close to the slow manifold in order to approximate the correct slow dynamics with acceptable precision. As the slow manifold is not explicitly known, the lifting operator maps not exactly on the slow manifold, a direct numerical evaluation of the macroscopic behaviour after the lifting yields the dynamical behaviour near the low-dimensional manifold $\mathcal{C}$. To compensate this lifting error, typically a healing step with healing time t_{heal} is introduced for converging closer to the attractive slow manifold, in cost of being at a different position in phase space. To compensate for this, C. Marschler et al. introduced an implicit approach [70–72]. In details, this approach leads to solving the implicit equation

$$\mathcal{R}(\Phi(t_{\text{heal}}, \mathcal{L}(V))) = \mathcal{R}(\Phi(t_{\text{heal}} + \delta, \mathcal{L}(U))) \tag{1}$$

with respect to V which implicitly defines the time-δ map $\tilde{\mathcal{P}}(\delta, U) : U \mapsto V$ of U by comparing healed quantities; see Fig. 1.

Despite the fact, that finding a suitable t_{heal} that compensates the lifting error is a tedious task, it is highly rewarding, since in general it is typically impossible to construct a lifting $\mathcal{L}$ which maps precisely onto the slow manifold $\mathcal{C}$. Whereas short healing times increase the systematic error, large healing times yield cancellation effects due to reaching the stationary point on the slow manifold $\mathcal{C}$. In order to solve the implicit equation iteratively (e.g. by Newton's method), the condition $\text{rg}\mathcal{R} \subseteq \text{dom}\mathcal{L}$ has to hold. In the following, we will discuss how the

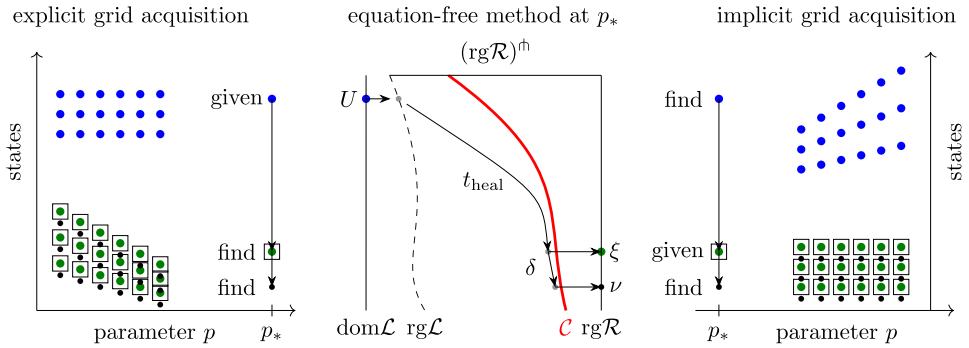

Fig. 2 Comparison of the data acquisition using an explicit (left) and implicit scheme (right). For an explicit approach, an unhealed state ● (U) is chosen. By applying the lift–evolve–restrict scheme, at some parameter p_*, for times t_{heal} and $t_{\mathrm{heal}} + \delta$, we can access the healed state ● (ξ), and the healed state ● (ν), respectively. Subsequently, we can approximate the derivative □ ($F(\xi)$) using Eq. (2). For the implicit approach, a healed state ● (ξ) is chosen and we use Eq. (3) to determine the unhealed state ● (U) for some parameter p_*. By applying the lift–evolve–restrict scheme for $t_{\mathrm{heal}} + \delta$, we obtain the healed state ●(ν) and can approximate the derivative □ ($F(\xi)$) at the chosen state ● (ξ)

equation-free framework can be used to approximate the macroscopic dynamics at desired points in macroscopic phase space for the construction of a Gaussian process model.

2.2 Equation-free sampling for Gaussian process regression

The aim is to construct a macroscopic model which provides information about the macroscopic dynamics at specific points in phase space. This model enables us to study the macroscopic behaviour of the system, for instance the parameter-dependent changes in qualitative behaviour. Instead of a direct equation-free bifurcation analysis by computing several points of the bifurcation diagram locally, the Gaussian process model provides an alternative approach, which solely uses a few local results of the equation-free approach, distributed in the macroscopic phase space, to gain information of the vector field in the region of interest. By applying the multidimensional bisection method or alternative zero-problem solvers at out-of-sample positions and the corresponding evaluations of the vector field, we are able to gain a bifurcation diagram including uncertainty quantification due to the probabilistic nature of the model.

The success of Gaussian process regression relies on the positions, and therefore the well-coverage or sparsity, of the sampling points in the macroscopic phase space and the quality of the vector field information. In order to obtain the derivative information in the explicit approach, we would consider a specific point in phase space U, e.g. from a regular grid. Applying the lift–evolve–restrict scheme for times t_{heal} and $t_{\mathrm{heal}} + \delta$ enables the approximation of the time derivative at the healed state $\xi = \mathcal{R}(\Phi(t_{\mathrm{heal}}, \mathcal{L}(U)))$ via the forward difference scheme

$$F(\xi) = \frac{\mathcal{R}(\Phi(t_{\mathrm{heal}} + \delta, \mathcal{L}(U))) - \xi}{\delta}, \tag{2}$$

see also Fig. 1. When using an explicit approach, we can either obtain high-quality derivative information at a healed state ξ, which is unknown beforehand and different from the chosen point U, or treat the derivative $F(\xi)$ from Eq. (2) as an approximation for $F(U)$; see also Ref. [65]. In the first option, the quality of vector field evaluations is ensured but leads to a distortion of the sampling grid (also referred to as training grid), i.e. the approximation of derivatives at ξ; see Fig. 2, left column.

This can heavily impact the sampling grid, possibly leaving out some areas of interest in the macroscopic phase space. In contrast, the second option regains the desired grid point positions at cost of the quality of the derivative information. An implicit equation-free approach solves both problems at once, delivering high-quality derivative information at the chosen positions in the macroscopic phase space.

2.3 Generating data at desired macroscopic points with an implicit equation-free approach

In contrast to the previous explicit approach, we now select an already healed state ξ in the macroscopic phase space and use an implicit equation to match a corresponding unhealed state U,

$$\mathcal{R}(\Phi(t_{\mathrm{heal}}, \mathcal{L}(U))) = \xi. \tag{3}$$

This equation stems from a technique which is called *matching the restriction* [70, 71], where it is used to find a microscopic configuration corresponding to the healed macro-state ξ. For a given ξ, we solve equation (3) with respect to U (e.g. by NEWTONs method) yielding the corresponding unhealed state U. Applying the lift–evolve–restrict scheme to U for the time $t_{\text{heal}} + \delta$ enables the approximation of the derivative at ξ just as in Eq. (2). This implicit method circumvents the distortion of the grid, since we can compute the unhealed state U for any given healed state ξ from the defined macroscopic phase space. This highlights the advantage of the implicit approach in contrast to the explicit approach. Figure 2 summarises the distorting behaviour, depicting on the left the explicit approach and on the right the implicit approach.

In this manner, we collect state-derivative pairs $(\xi, F(\xi))$ and subsequently generate a data set M, which will be used in Sect. 2.4 for Gaussian process regression. Despite the fact that the computationally expensive evaluations were performed at solely a finite number of selected points in the macroscopic phase space, with Gaussian process regression, we are able to predict a global macroscopic model from the used data set M.

2.4 Gaussian process regression

Gaussian process regression (GPR) can be used to find nonlinear relations in data [69, 79, 80]. In the context of machine learning, GPR belongs to the supervised learning techniques. The given (regression) problem is to model an unknown function $F : \mathbb{R}^N \to \mathbb{R}$ for which only a limited set of data $M = \{(x_i, y_i) \mid x_i \in \mathbb{R}^N,\ y_i \in \mathbb{R},\ i = 1, \ldots, D\}$ with inputs $x_1, \ldots, x_D$ stored in a matrix $X = [x_1, \ldots, x_D] \in \mathbb{R}^{N \times D}$ and disturbed function values $y_i = F(x_i) + \epsilon_i$ summarised in the vector $y \in \mathbb{R}^D$ is given. The outputs y_i are assumed to be disturbed by some independent and identically distributed (i.i.d.) Gaussian noise ϵ_i with zero mean and variance σ^2.

In GPR, the unknown function F is assumed to be distributed as a Gaussian process (written as $F \sim \mathcal{GP}(m, k)$) with mean function m, here set to be the zero function and covariance function k, also called kernel function; for details, see, e.g. Refs. [69, 79, 81, 82]. Considering the data set M and a zero mean function m, predictions in Gaussian process regression are based upon the choice of an appropriate kernel function k and hyperparameters, including σ^2. Optimal hyperparameters can be determined by maximising the log marginal likelihood [69], depending on the known outputs y and inputs X,

$$\log p(y|X) = -\frac{1}{2} y^T (K + \sigma^2 I)^{-1} y - \frac{1}{2} \log |K + \sigma^2 I| - \frac{D}{2} \log 2\pi,$$

where I denotes the $D \times D$ identity matrix and $K \in \mathbb{R}^{D \times D}$ is the covariance or kernel matrix with entries $K_{ij} = k(x_i, x_j)\ \forall i, j = 1, \ldots, D$. In general, the log marginal likelihood can have several local maxima, leading to different results depending on the initial values for the hyperparameters and the chosen optimisation routine. See also Ref. [83] for an automatic calculation of initial values directly from data.

Considering some previously not seen inputs, so-called out-of-sample points, $\tilde{x}_1, \ldots, \tilde{x}_{\tilde{D}}$ summarised in a matrix $\tilde{X} = [\tilde{x}_1, \ldots, \tilde{x}_{\tilde{D}}] \in \mathbb{R}^{N \times \tilde{D}}$, predictions can be made by deriving the conditional distribution from the joint distribution of $F(X) = (F(x_1), \ldots, F(x_D))^T$ and $F(\tilde{X}) = (F(\tilde{x}_1), \ldots, F(\tilde{x}_{\tilde{D}}))^T$. The joint distribution of $F(X)$ and $F(\tilde{X})$ follows a multivariate Gaussian distribution, from which the conditional distribution of the unknown outputs $F(\tilde{X})$ given the data y, X and the out-of-sample points $\tilde{X}$

$$F(\tilde{X}) \mid y, X, \tilde{X} \sim \mathcal{N}(\mu_{\text{PD}}, \Sigma_{\text{PD}})$$

is obtained. Predictions are performed with the conditional or posterior mean μ_{PD} and posterior covariance Σ_{PD}

$$\mu_{\text{PD}} = K_*^T (K + \sigma^2 I)^{-1} y \tag{4}$$

$$\Sigma_{\text{PD}} = K_{**} - K_*^T (K + \sigma^2 I)^{-1} K_*, \tag{5}$$

with the covariance matrices $K_{**} \in \mathbb{R}^{\tilde{D} \times \tilde{D}}$ and $K_* \in \mathbb{R}^{D \times \tilde{D}}$ constructed in the same manner as K. In the following, we use the term GP model to refer to the posterior mean μ_{PD} and covariance Σ_{PD} given by Eqs. (4)–(5) with optimised hyperparameters of the kernel function. Together with the equation-free approaches presented in Sects. 2.2 and 2.3, we use GPR to construct a model of the macroscopic right-hand side of a microscopic defined system bridging both methods.

3 Application to a large-scale neural system with integrate-and-fire neurons

In this section, we aim to apply the ideas described in the previous section to a high-dimensional system of integrate-and-fire neurons introduced in Sect. 3.1. We provide a detailed explanation, not only on how to construct a model for the macroscopic dynamics; see Sect. 3.2, but also on how to use the model for a macroscopic bifurcation analysis in Sect. 3.3. We compare our bifurcation analysis obtained by a GP model with pseudo-arclength methods in Sect. 3.4.

3.1 Description of the neural network model

For reasons of comparison, we apply the methods from Sect. 2 to a system of N integrate-and-fire neurons, previously investigated in Ref. [65]. The dynamics of a single neuron are described by the two equations:

$$\frac{\mathrm{d}V_i}{\mathrm{d}t} = I - V_i + \omega_i + \frac{1}{N}\sum_{j=1}^{N} s_j - \sum_k \delta(t - t_{ik}) \tag{6}$$

$$\tau \frac{\mathrm{d}s_i}{\mathrm{d}t} = -s_i + A\sum_k \delta(t - t_{ik})(1 - s_i), \tag{7}$$

where the first equation represents the dynamics of the membrane potential V_i, while the second represents the dynamics of the synaptic activity s_i of the i-th neuron. The spiking time t_{ik} denotes the k-th spiking event of the i-th neuron. That is, the membrane potential V_i reaches the threshold $V_i = 1$ of the i-th neuron for the k-th time. The Dirac δ distribution in Eq. (6) resets the membrane potential to zero at each spiking event. Similarly in Eq. (7), the synaptic activity gets additionally adjusted by the coupling term at each spiking event. The investigation of the network is carried out for $N = 200$ neurons. The choice of 200 neurons is a compromise between computational time and averaging effects by taking the mean. As discussed in Ref. [65], the number of neurons could be chosen differently and in particular much smaller, assuming that the number of realisations is larger to obtain smooth results. For all 200 neurons, the parameter $A = 0.4$ represents the connectivity between the neurons, $\tau = 50$ ensures the separation of time scales and I is an external current serving as the bifurcation parameter. Furthermore, Eq. (6) shows all-to-all connectivity. The membrane potential of each neuron is additionally disturbed by some uncorrelated Gaussian white noise with $\omega_i \sim \mathcal{N}(0, \sigma^2)$ and $\sigma = 0.0245$. The effect of the intrinsic system noise on the macroscopic behaviour is further discussed in appendix A.1.

For the equation-free approach, we have to identify a suitable macroscopic state to describe the full network. Indeed, this problem can be solved by applying (non-)linear dimension reduction methods or manifold learning; see, e.g. Refs. [73, 78, 84] to gain a macroscopic state as mentioned in Sect. 2.1. In our example, we follow Ref. [65] and choose for simplicity and benchmarking purposes the mean synaptic activity

$$S = \frac{1}{N}\sum_{j=1}^{N} s_j$$

of all synaptic activities s_j as the macroscopic variable. The mean synaptic activity S is also relevant for medical reasons, as it can be directly related to the local field potentials that are measured in medicine [85, 86]. This makes it an even more attractive choice as the macroscopic variable. Consequently, we assume that the network dynamics can be described by an ordinary differential equation of the form $\dot{S} = F(S, I)$. The restriction operator $\mathcal{R}$ within the equation-free framework is given by taking the mean of the synaptic activities, whereas the lifting operator $\mathcal{L}$ is chosen such that it maps a given macroscopic state S to the microscopic scale via $\mathcal{L}(S) = (V_i, s_i)$ where $V_i \sim \mathcal{U}(0, 1)$ and $s_i = S\ \forall i = 1, \ldots, N$. We integrate the microscopic Eqs. (6)–(7) with the Euler–Maruyama method [87] with fixed time steps $\Delta t = 0.01$. For further details on the implementation, we would like to refer to the open source code [88].

For a certain parameter range, the system (6)–(7) shows bistability on the macroscopic scale, with one low and one high activity state, as shown in Fig. 3. A quasi-stationary up and down sweep of the system, obtained by averaging over the last 2000 time steps, shows two branch switching events, from the high to the low activity state and vice versa indicating a hysteresis, as shown in the left column in Fig. 4. In the following, we perform an investigation of the stationary solutions with our proposed framework from Sects. 2.2 and 2.3.

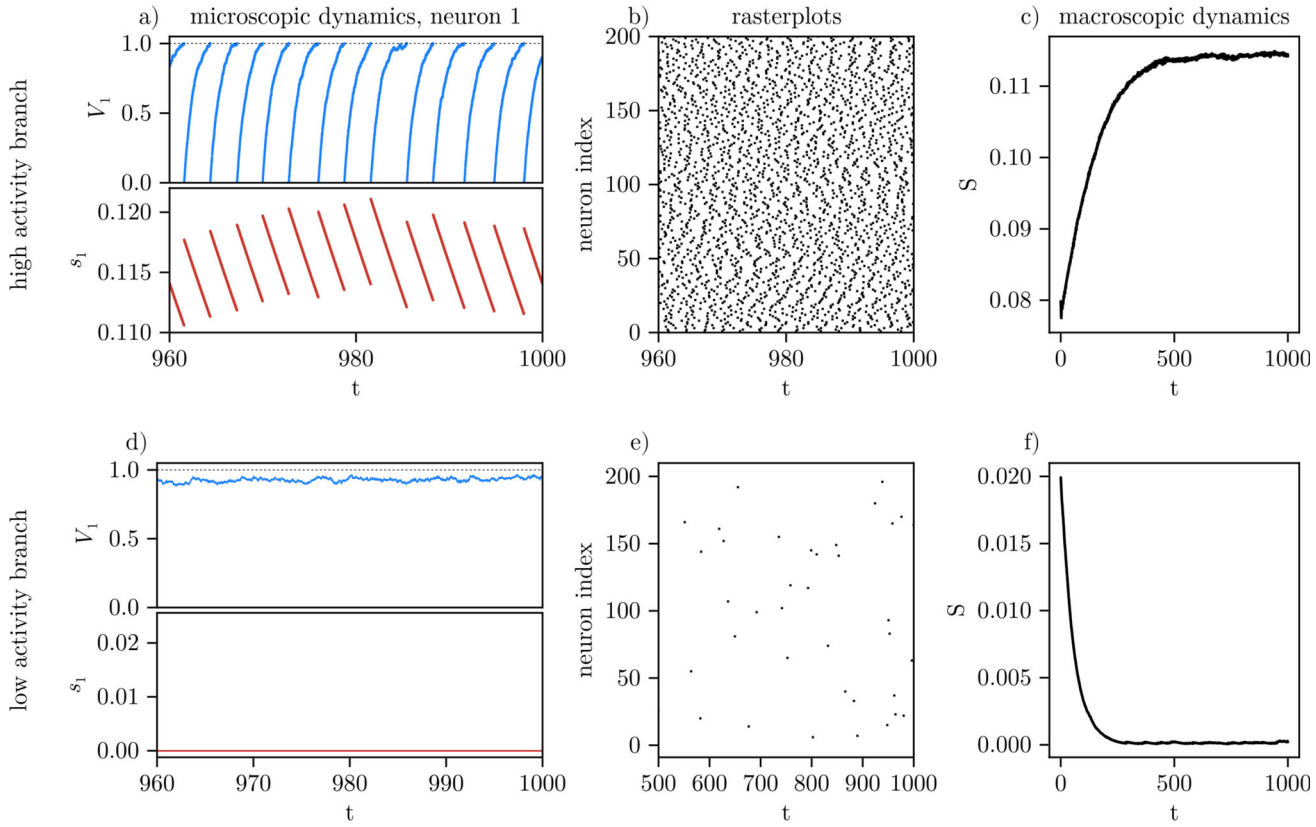

Fig. 3 Demonstration of the bistable regime for the mean synaptic activity S. For $I = 0.93$, we find one high and one low-activity stable state for S; see **c** and **f**. The steady-state behaviour of the microscopic dynamics for the first neuron can be seen in **a** and **d**. Whereas in the high activity branch, the membrane potential reaches the threshold frequently and spiking events occur; in the low-activity branch, the membrane potential does not reach the threshold $V = 1$, resulting in the low or even zero synaptic activity of the individual neuron. The spiking events themselves are visualised for each neuron in so-called raster plots in **b** and **e**. At the beginning of each integration step, we check if a neuron surpassed the threshold $V = 1$. If so, we save the corresponding index of the neuron at the time before the integration step. The times and indices of those spiking events are shown as black points in figure **b** and **e**, which also show the different firing rates of the two stable states. In **b**, we show the raster plot for the last 40 time units and in **d** for the last 500 time units. The micro-configuration of the system was chosen according to the lifting operator described in the text with $S = 0.08$ in **a**–**c** and $S = 0.02$ in **d**–**f**

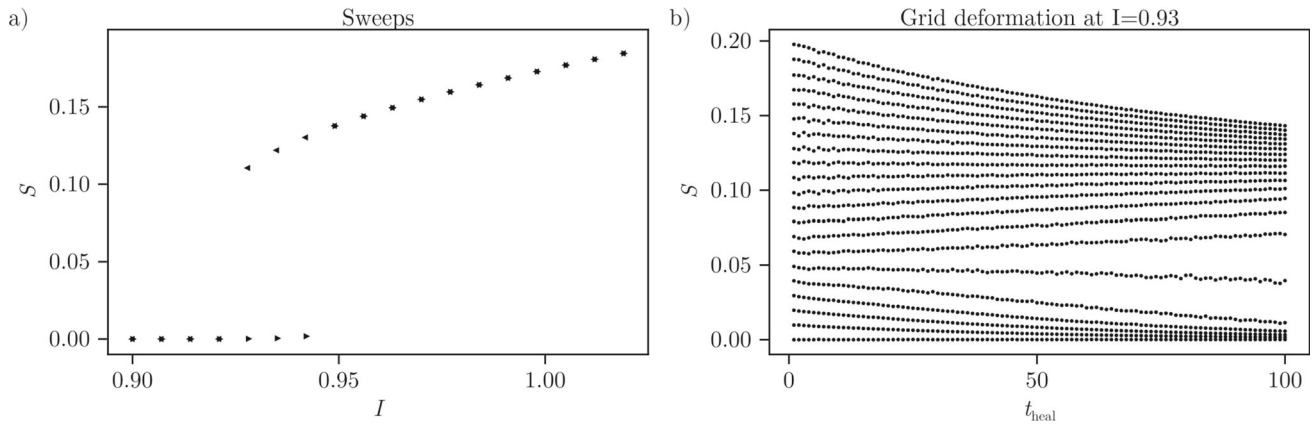

Fig. 4 **a** Depiction of forward (right oriented triangle ▶) and backward (◀) sweeps, showcasing the bistable regime of the macroscopic mean synaptic activity S of the network of integrate-and-fire neurons. **b** Effect of distortion of a regular grid in the macroscopic phase space for the mean synaptic activity S due to different healing times. A not too small healing time is required to guarantee the convergence to the slow manifold after microscopic initialisation via the lifting. For larger healing times, the initially evenly spaced states S separate according to the evolution in phase space. This consequently leads to gaps in the data acquisition required for the Gaussian process regression

3.2 Construction of the Gaussian process model

To demonstrate the effect of grid distortion in the explicit approach and justify the use of the implicit method, we show how linearly spaced initial values of S, corresponding to U in Figs. 1 and 2, are deformed at $I = 0.93$ for various healing times. The right column in Fig. 4 shows the effect of different healing times for 21 evenly spaced initial states from the interval [0, 0.2]. For larger healing times, we see that some states tend towards the upper stable stationary solutions, while some tend towards the lower stable solution. Consequently, we would miss information apart from the stable solutions, resulting in a neighbourhood with many data points and sparse data representatives. Larger healing times result in closer proximity of the slow manifold, effectively magnifying the grid distortion, whereas shorter healing times would lead to derivative information away from the slow manifold. The implicit approach proposed in Sect. 2.3 circumvents this problem and will be the method of choice. In Sects. 3.3 and 3.4, we will compare two GP models, constructed with data obtained by the explicit approach from Sect. 2.2 and the implicit approach from Sect. 2.3.

For the explicit approach, we first take a macro-state S, referred to as U in Fig. 2, from the chosen unhealed grid. We then apply the lift–evolve–restrict scheme for $t_{\text{heal}} = 40$ and $t_{\text{heal}} + \delta = 50$ and use Eq. (2) to approximate the derivative $F(\xi)$ at the healed state ξ. In the implicit approach, we approximate derivatives by first solving Eq. (3) with respect to the unhealed state U, using the given healed state $\xi = S$ and $t_{\text{heal}} = 40$. Setting $\delta = 10$ in Eq. (2) gives us an estimate for the macroscopic derivative $F(\xi)$. Due to the stochastic nature of the microsystem, we applied the lift–evolve–restrict scheme to an ensemble of 30 realisations, averaging the macro-states for both the implicit and explicit approach. To obtain the parameter-dependent behaviour on the macroscopic scale in a bifurcation diagram, we consider pairs (I, S) consisting of a parameter I and a state S. Together with the respective derivative approximations, this generates the data set M for the Gaussian process regression. In the considered example, 21 initial states S evenly spaced in the interval $I \in [0, 0.2]$ are selected, similarly to Fig. 4. For the parameter I, 27 equidistant values from the interval [0.9, 1.03] are used.

To obtain the GP models, the *GaussianProcesses.jl* package [89] is used. Hereby, the following specifications are chosen: a zero mean function, see Sect. 2.4, and the squared exponential kernel function

$$k(x, x') = \eta^2 \exp(-(x - x')^T (x - x')/(2l^2)),$$

containing two hyperparameters η and l, which are optimised by the *Optim.jl* package [90]. We use a unit range transformation, also called min–max scaling, to preprocess the elements of the data set M. This transformation maps the data points, i.e. the macro-states, parameters and derivatives on the unit interval [0, 1]. An additional rescaling of the elements of M to have zero mean could be done. This will be discussed in Sect. 3.3 and is further investigated in the Appendix. After applying the preprocessing, the hyperparameters are found by maximising the log marginal likelihood presented in Sect. 2.4. Local maxima of the log marginal likelihood are found with the hyperparameters $l \approx 0.183$, $\eta \approx 0.301$ and a noise variance of approximately $3.359 \cdot 10^{-5}$ for the explicit approach and $l \approx 0.194$, $\eta \approx 0.274$ with a noise variance of $2.295 \cdot 10^{-5}$ for the implicit approach. The rescaled predictions, i.e. derivatives at out-of-sample points, made by the Gaussian process models can be found in Fig. 5.

The top row in Fig. 5 shows a depiction of the training points for the explicit a) and implicit b) approach as well as heat map representations of the resulting macroscopic model at out-of-sample points. Longer healing times in the explicit scheme imply points being in a proximity of the stable solutions, resulting in sparse sampling regions in the macroscopic phase space. The implicit scheme circumvents sparse sampling regions, resulting in an approximation of the macroscopic derivatives at the desired positions in macroscopic phase space.

3.3 Macroscopic bifurcation analysis

With the obtained parameter-dependent GP models $\dot{S} = F(S, I)$ for the macroscopic right-hand side of the mean synaptic activity S, we now aim to perform a bifurcation analysis on the macroscopic scale. This is accomplished by finding the zero level sets, i.e. the parameter-dependent stationary solutions, of the GP model within the parameter range $I \in [0.9, 1.03]$, which is achieved by the multidimensional bisection method from the *MDBM.jl* package [91]. An alternative method could be to apply a numerical continuation such as the pseudo-arclength continuation [92] on the GP model for $F(S, I)$. To visualise the heat maps in Fig. 5 and as an initial grid for the multidimensional bisection method, we use an equally spaced 250×250 grid of out-of-sample points $\tilde{X}$, bounded by the minima and maxima of the sampling set M. The iterative bisection algorithm leads to resolution doubling in each step near the zero level set, which results in a new $\tilde{X}$. After 3 iterations, we approximate the parameter-dependent stationary solutions or so-called branches.

The stable branches of the bifurcation diagram obtained by the multidimensional bisection method are in accordance with the sweeps previously shown in Fig. 4. In addition, an unstable branch connecting the stable branches is revealed, substantiating the suspected hysteresis; see the lower row in Fig. 5. In Fig. 5, we also show the computed eigenvalue for different parameters I, i.e. the derivative of the right-hand side $F(S, I)$ with

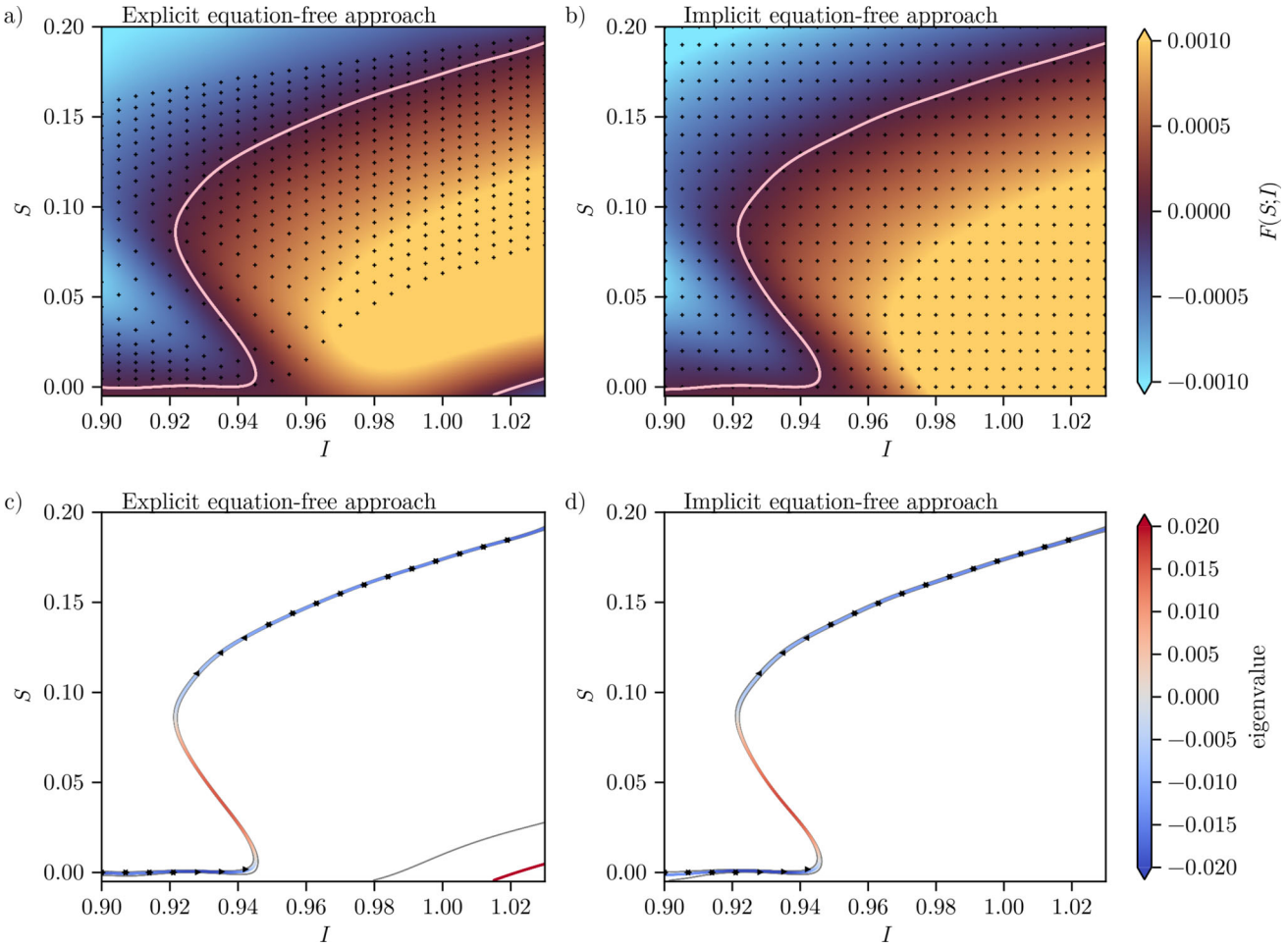

Fig. 5 Macroscopic bifurcation diagram obtained by GP models for the macroscopic right-hand side. The stationary states of the macroscopic mean synaptic activity S are shown depending on the input current I. Left column, **a**, **c**: the results of the explicit equation-free approach. Right column, **b**, **d**: the results of the implicit equation-free approach. Upper row, **a**, **b**: the sampling grid, the obtained macroscopic vector field (right-hand side, RHS, as heat map) of the GP model, as well the macroscopic stationary states S. Lower row, **c**, **d**: macroscopic bifurcation analysis of the macroscopic state S including stability properties and 95% confidence intervals of the GP model. The two stable branches, which are confirmed by a quasi-stationary up (right oriented triangle ►) and down (left oriented triangle ◄) sweep, are connected by an unstable branch. The explicit approach shows spurious stationary states due to the gap in the sampling grid, while the implicit approach shows no artefacts. This is in correspondence to the grids shown in the upper row. A quantification of uncertainty is shown by an approximation for the 95% confidence intervals. These confidence intervals get smaller when more data points are available in this area. This explains the slightly smaller uncertainty in the explicit approach as in a neighbourhood of the attractive stable states data points are accumulated (see also Fig. 4) in the distorted grid

respect to S at the stationary solutions, approximated by a forward difference. The zeroes indicate the positions of the bifurcation points. As depicted in Sect. 2.4, the GP model uses the mean of the posterior distribution as a prediction, while it also serves us the covariance, which we can be used to determine confidence intervals in the bifurcation diagram. This is achieved again using the multidimensional bisection method but this time applied to the upper and lower bound of the 95% confidence interval, here approximated by the mean plus or minus two times the standard deviation (see also Eqs. (4)–(5)). As shown in the graphics, the uncertainty is quite small due to the optimisation of hyperparameters.

Both GP models, explicit and implicit, from Sect. 3.2 show good results regarding the bifurcation analysis. However, the grid distortion in the explicit approach leads to resulting sparse data regions in some parts of the phase space, e.g. for large I and small S values. In fact, a consequence of the sparsity are spurious states as well as confidence bounds appearing in the bifurcation diagram shown in Fig. 5. We observe that we can slightly increase the model accuracy of the explicit approach outside the sampling grid by additionally rescaling the elements of the data set M to have zero mean as mentioned in the previous section. However, the predicted spurious upper

confidence bound remains, confirming the necessity of the implicit approach which circumvents the grid distortion as shown in Appendix A.2.

3.4 Comparison to equation-free pseudo-arclength continuation

We compare our bifurcation diagram obtained by the implicit GP modelling approach, presented in the previous section to two equation-free approaches, the explicit and implicit one. First, we compare with the results in Ref. [65], which are based on an explicit equation-free scheme. Second, we use an implicit approach [70–72], presented in Sect. 2.1.

In the approach of C. Laing [65], the macroscopic right-hand side $F(S(0), I)$ is approximated: Given an initial macroscopic state $S(0)$, the lift–evolve–restrict scheme $P(\delta_{\max}, S(0))$ with $\delta_{\max} = 20$ is applied. Using of the restriction operator $\mathcal{R}$ at different time points in the time interval [10, 20] yields a time series. It is assumed that the slope of a linear regression for $t \in [10, 20]$ can be used to approximate the macroscopic right-hand side at $S(0)$. This is repeated for 64 realisations with the average of the slopes as a final approximation of $F(S(0), I)$. Stationary solutions of S are now calculated by a pseudo-arclength continuation; see Fig. 6a).

The second approach solves the implicit Eq. (1) with $U = V$. Thus, we search for the state U that satisfies [70, 71]

$$\frac{1}{\delta}[\mathcal{R}(\Phi(t_{\text{heal}} + \delta, \mathcal{L}(U))) - \mathcal{R}(\Phi(t_{\text{heal}}, \mathcal{L}(U)))] = 0. \tag{8}$$

Again the upper expression is calculated 64 times and the average is used in the continuation algorithm. Figure 6 shows the bifurcation diagram obtained with this approach for $t_{\text{heal}} = 40$ and $\delta = 30$. Figure 6 shows the healed values, i.e. we take the results of Newtons method (i.e. U in Eq. (8)) and reapply the lift–evolve–restrict scheme. Due to the noise, we average over 64 realisations. To perform the continuation around the saddle-node bifurcation points, a pseudo-arclength continuation [92] is used. The stability information of the branches in the implicit scheme can be acquired, see Ref. [70], by solving for the time discrete eigenvalues μ of the generalised eigenvalue problem

$$[\partial_x(\mathcal{R}(\Phi(t_{\text{heal}} + \delta, \mathcal{L}(x)))|_{x=U}]x = \mu[\partial_x(\mathcal{R}(\Phi(t_{\text{heal}}, \mathcal{L}(x)))|_{x=U}]x,$$

which can be obtained by linearizing the implicit flow around U. Hereby, forward finite differences are used with $\delta x = 5 \cdot 10^{-3}$. Time continuous eigenvalues can afterwards be gained by $\lambda = \frac{1}{\delta} \log \mu$.

The resulting bifurcation diagram of the implicit approach outperforms the one of the explicit approach. The branches of both diagrams align well with the results of the sweep. Figure 6 also shows the bifurcation diagram from the GP model based on the implicit approach in Sect. 3.3 (see also Fig. 5). We see a good agreement between all three lines.

Better lifting operators could further improve the results, especially the ones from the explicit approach as demonstrated in Ref. [65]. Nevertheless, for a better comparison, we stick to our lifting operator. The reason for the better results using the implicit approach is that the derivative information is computed at the desired position in phase space. Therefore, the resulting bifurcation diagram is of higher precision.

4 Conclusion, discussion and outlook

We derived a model for the macroscopic dynamics of a network of integrate-and-fire neurons, by generating training data with an explicit and implicit equation-free approach [63, 71, 72], frameworks which have been proven to be powerful numerical tools for the analysis of macroscopic dynamics. The implicit approach allows the evaluation of macroscopic dynamics at desired points in phase space, whereas in the explicit approach, the points of evaluation are shifted. Using Gaussian process regression [69, 79, 80], we inferred a probabilistic model directly from the generated data without the necessity of choosing a set of basis or library functions. The model, obtained by combining the data acquisition precisely at the desired positions in phase space by an implicit equation-free approach and GPR, was used to study the long-term dynamics by performing a macroscopic bifurcation analysis including stability properties and a quantification of uncertainty. The bifurcation diagram of the GP model based on the implicit approach aligns well with the results of both, an explicit and implicit equation-free pseudo-arclength approach as well as a quasi-stationary up and down sweep.

Our derivative approximation based on the implicit scheme enhances the accuracy of derivative estimation, leading to a more reliable macroscopic approximation. Since recent machine learning approaches, such as physics-informed neural networks (PINNs) [37, 44], rely on automatic derivative estimation, our approach may open new

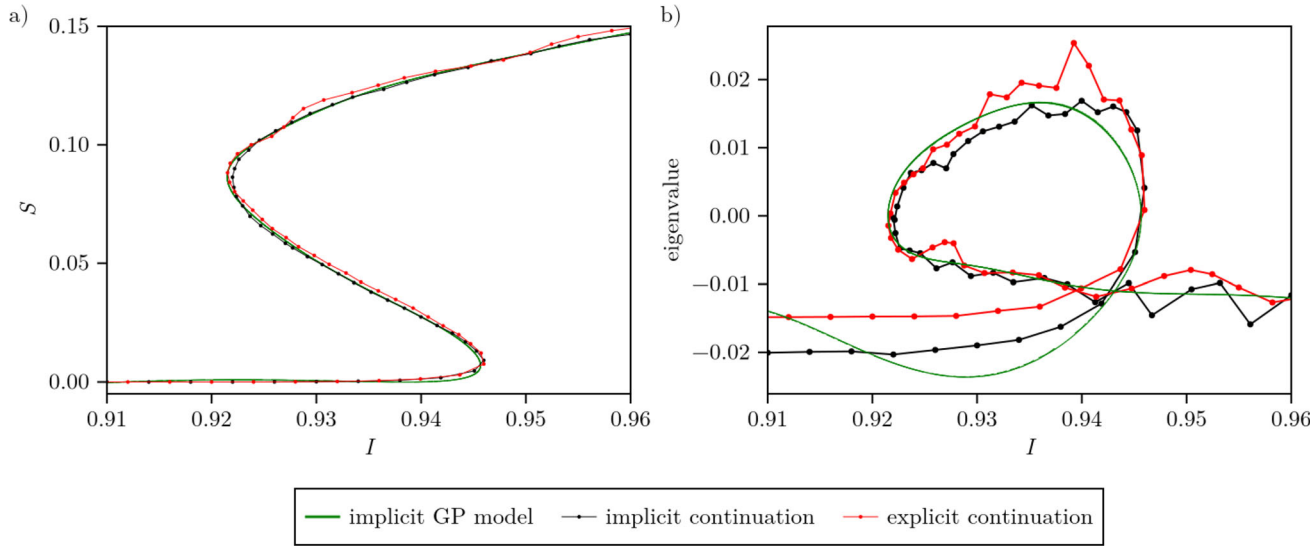

Fig. 6 **a** Bifurcation diagrams for the macroscopic state S using an explicit approach (red) presented in Ref. [65], an implicit approach (blue) and the results of the GP model (green) with the data sampled by an implicit equation-free approach. The equation-free curves are obtained by a pseudo-arclength continuation with adaptive predictor step size. **b** Stability information for the found stationary states shown in (**a**). A state derivative greater than zero corresponds to unstable states whereas stable stationary states have a negative state derivative

directions for the development of surrogate models. Another promising line of research is the application to realistic brain network models. A concrete example arises in the basal ganglia network, a network of interconnected regions responsible for motor control and implicated in movement disorders such as Parkinson's disease and dystonia [93–96]. In this network, the macroscopic dynamics are experimentally accessible and are typically expressed as local field potentials, which are related to the mean synaptic activity used in this work [85, 86]. The proposed approach is well suited for analysing these macroscopic dynamics and for uncovering qualitative change in the macroscopic behaviour.

In the future, we intend to utilise the global information of the GP model, i.e. the macroscopic dynamics to enable control of complex systems. Upcoming studies could focus on improvements regarding the implicit equation-free approach, e.g. by introducing mutable healing times or applying high-order finite-difference schemes to approximate macroscopic dynamics. In the present work, we solely used a regular sampling grid in the implicit approach, but we would like to emphasise that other choices of sampling grids are possible enabling problem- and area-specific choices of sampling points in the macroscopic phase space. In the specific task of bifurcation analysis, it may be practicable to first perform a regular scan of the phase space and possibly add sampling data, in a similar fashion to the multidimensional bisection method, yielding resolution doubling in the proximity of branches. This should result in smaller confidence intervals, which may even outperform the ones of the explicit approach. Even though we only showed our framework in the case of a one-dimensional macro-state, it is possible to extend the approach to a higher dimensional setting, either by constructing a GP model for each macro-state or by considering vector-valued kernel functions [97].

Acknowledgements The research of TS, HW, KS and JS has been funded by the Deutsche Forschungsgemeinschaft (DFG, German Research Foundation) SFB 1270/2 "Electrically active Implants" 29915058. TS and HW wish to express their gratitude to CS for their hospitality during their stay in Naples. TS would furthermore like to thank the European Union and the Erasmus+ program for the opportunity to stay in Naples for the majority of his master's thesis.

Author contribution statement

Conceptualisation and methodology [TS, HW, KS, CS, JS]; formal analysis and investigation [TS, HW]; writing—original draft preparation: [TS, HW]; writing—review and editing [TS, HW, KS, CS, JS]; funding acquisition: [JS]; supervision: [KS, CS, JS].

Funding Open Access funding enabled and organized by Projekt DEAL.

Data Availability Data sets and code generated during the current study are available on Zenodo [88].

Declarations

Conflict of interest The authors have no conflict of interest to declare that are relevant to the content of this article.

Appendix

Testing the robustness of macroscopic models against intrinsic system noise

The intrinsic system noise ω_i with $\sigma = 0.0245$, used in the main text, has a large effect on the resulting macroscopic behaviour. To test the robustness of our approach against different noise levels, Fig. 7 shows resulting macroscopic right-hand sides and bifurcation diagrams including stability information for the implicit sampling approach for different noise levels $\sigma \in \{0.035, 0.049, 0.07\}$. For each GP model, the same sampling points were used. The resulting bifurcation diagrams are again compared with a quasi-stationary up and down sweep of the system, averaged over the last 2000 time steps. For $\sigma = 0.035$, the hysteresis discussed in Sect. 3 still remains. Increasing the noise level makes the hysteresis in the observed parameter range disappear. The resulting bifurcation diagrams again correspond well with the sweeps. The slight shift between forward and backward sweep for some parameters is a result of the larger noise. The confidence intervals remain barely visible, demonstrating the robustness of the approach for larger systematic noise terms.

Discussion of data preprocessing

As discussed in Sects. 3.2 and 3.3, a min–max scaling was used to map all inputs and outputs to the unit interval $[0, 1]$. For the GP model and the results shown in Fig. 5, a zero mean function was used together with the squared exponential kernel function. A possible additional step is to rescale the inputs S, I and outputs $F(S, I)$ to have zero mean. This slightly increases the model accuracy outside the sampling grid as can be seen in Fig. 8. This especially benefits the explicit sampling approach due to the discussed grid distortion. Still, an artefact appearing as a spurious upper confidence bound in the bifurcation diagram remains.

The problem of grid distortion is not a method-specific problem of Gaussian process regression. Especially for systems, which require longer healing times, the explicit approach will not be able to capture parts of the sampling space, possibly leading to problems regardless of the used regression or modelling technique.

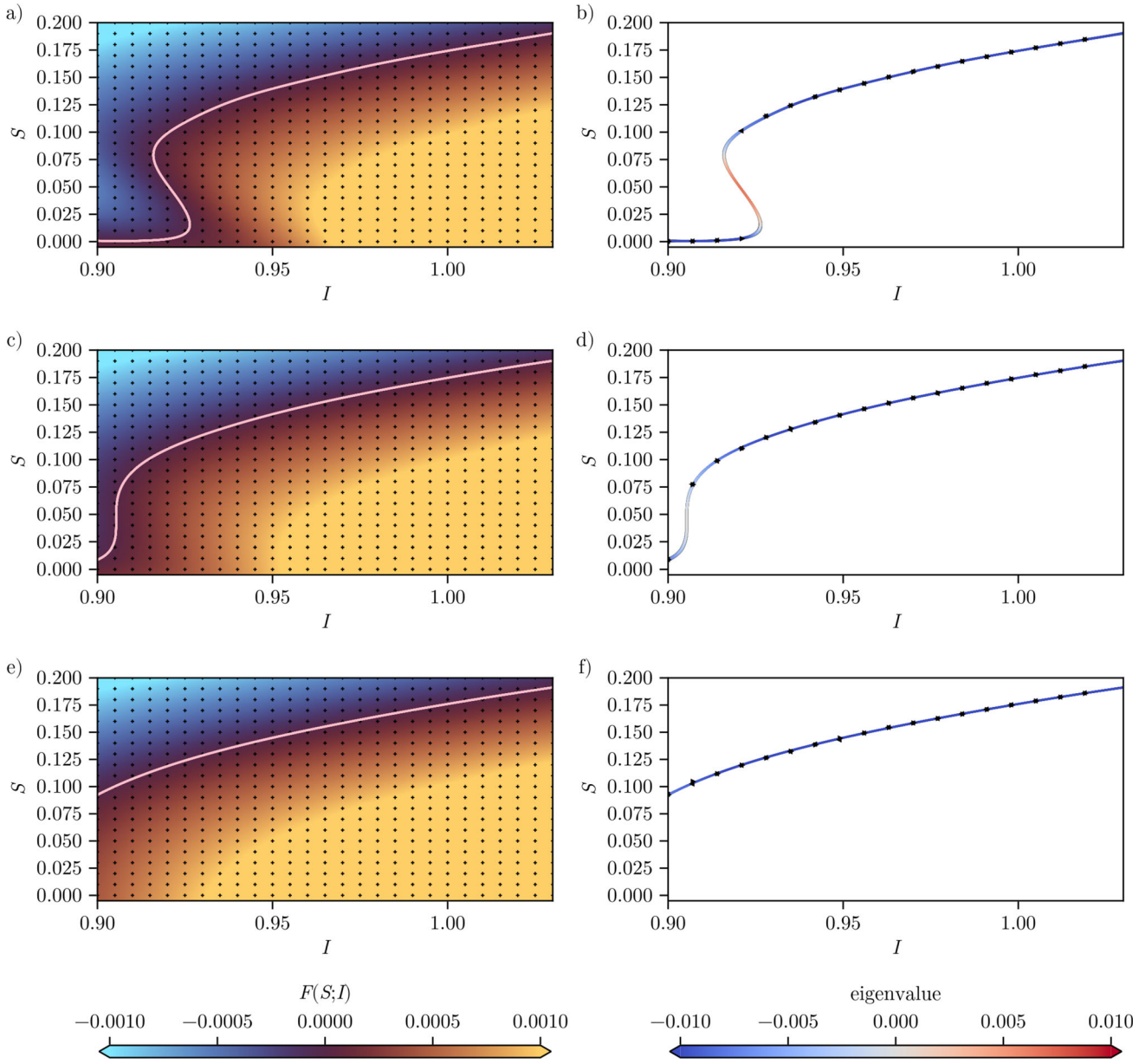

Fig. 7 Investigation of three different noise levels. Macroscopic right-hand sides $F(S, I)$ and bifurcation diagrams with stability information obtained from GP models using an implicit equation-free sampling approach. **a** and **b** Resulting right-hand side and bifurcation diagram for $\sigma = 0.035$, **c** and **d** for $\sigma = 0.049$ and **e** and **f** for $\sigma = 0.07$. The bifurcation diagrams in the right column are compared with quasi-stationary up (►) and down (◄) sweeps with the same noise

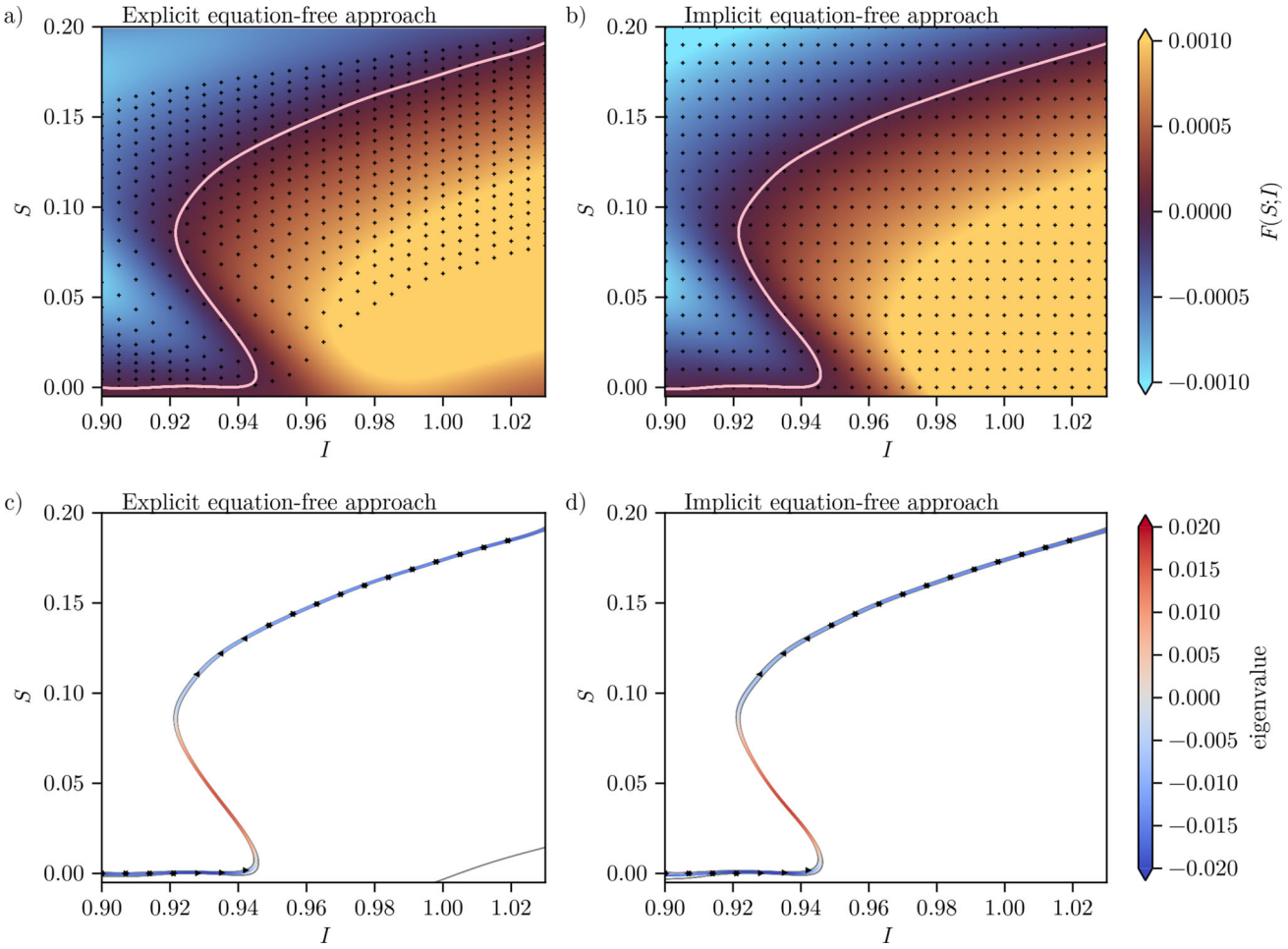

Fig. 8 Macroscopic right-hand side $F(S, I)$ and bifurcation diagram with stability information. For the GP model, a zero mean function and the squared exponential kernel was used. After rescaling the inputs and outputs on the unit interval, an additional step was performed to rescale the data to zero mean. Left column, **a**, **c** macroscopic model and bifurcation diagram obtained with an explicit equation-free sampling approach. Right column, **b d** macroscopic model and bifurcation diagram obtained with an implicit equation-free sampling approach. The resulting models and bifurcation diagrams align well with the ones shown in Fig. 5 in areas where sampling data is available. Due to the grid distortion in the explicit approach, the predictions in areas without any data differs from the ones shown in Fig. 5

References

1. R. Graham, H. Haken, Laserlight-first example of a second-order phase transition far away from thermal equilibrium. Z. Phys. **237**(1), 31–46 (1970). https://doi.org/10.1007/BF01400474
2. H. Haken, Synergetics: An Introduction (Springer. Berlin Heidelberg (1983). https://doi.org/10.1007/978-3-642-88338-5
3. H. Haken, Advanced Synergetics: Instability Hierarchies of Self-Organizing Systems and Devices (Springer. Berlin Heidelberg (1983). https://doi.org/10.1007/978-3-642-45553-7
4. C. Uhl, R. Friedrich, H. Haken, Analysis of spatiotemporal signals of complex systems. Phys. Rev. E **51**(5), 3890 (1995). https://doi.org/10.1103/PhysRevE.51.3890
5. R. Friedrich, S. Siegert, J. Peinke, S. Lück, M. Siefert, M. Lindemann, J. Raethjen, G. Deuschl, G. Pfister, Extracting model equations from experimental data. Phys. Lett. A **271**(3), 217–222 (2000). https://doi.org/10.1016/S0375-9601(00)00334-0
6. G. Deco, V.K. Jirsa, P.A. Robinson, M. Breakspear, K. Friston, The dynamic brain: from spiking neurons to neural masses and cortical fields. PLoS Comput. Biol. **4**(8), e1000092 (2008). https://doi.org/10.1371/journal.pcbi.1000092
7. V.K. Jirsa, H. Haken, Field theory of electromagnetic brain activity. Phys. Rev. Lett. **77**(5), 960 (1996). https://doi.org/10.1103/PhysRevLett.77.960
8. V.K. Jirsa, R. Friedrich, H. Haken, J.S. Kelso, A theoretical model of phase transitions in the human brain. Biol. Cybern. **71**(1), 27–35 (1994). https://doi.org/10.1007/BF00198909

9. T.D. Frank, A. Daffertshofer, C. Peper, P.J. Beek, H. Haken, Towards a comprehensive theory of brain activity: Coupled oscillator systems under external forces. Physica D **144**(1–2), 62–86 (2000). https://doi.org/10.1016/S0167-2789(00)00071-3
10. H. Haken, Brain Dynamics: An Introduction to Models and Simulations (Springer. Berlin Heidelberg (2008). https://doi.org/10.1007/978-3-540-75238-7
11. R. Chaudhuri, B. Gerçek, B. Pandey, A. Peyrache, I. Fiete, The intrinsic attractor manifold and population dynamics of a canonical cognitive circuit across waking and sleep. Nat. Neurosci. **22**, 1512–1520 (2019). https://doi.org/10.1038/s41593-019-0460-x
12. N. Fenichel, Geometric singular perturbation theory for ordinary differential equations. J. Differential Equations **31**(1), 53–98 (1979). https://doi.org/10.1016/0022-0396(79)90152-9
13. J.E. Rubin, D. Terman, in *Handbook of Dynamical Systems*, *Handbook of Dynamical Systems*, vol. 2, ed. by B. Fiedler (Elsevier Science, 2002), pp. 93–146. https://doi.org/10.1016/S1874-575X(02)80024-8
14. G.B. Ermentrout, D.H. Terman, Mathematical Foundations of Neuroscience (Springer. N. Y.) (2010). https://doi.org/10.1007/978-0-387-87708-2
15. V.K. Jirsa, W.C. Stacey, P.P. Quilichini, A.I. Ivanov, C. Bernard, On the nature of seizure dynamics. Brain **137**(8), 2210–2230 (2014). https://doi.org/10.1093/brain/awu133
16. E. Köksal Ersöz, J. Modolo, F. Bartolomei, F. Wendling, Neural mass modeling of slow-fast dynamics of seizure initiation and abortion. PLOS Computational Biology **16**(11), 1–31 (2020). https://doi.org/10.1371/journal.pcbi.1008430
17. C.W. Gear, T.J. Kaper, I.G. Kevrekidis, A. Zagaris, Projecting to a slow manifold: Singularly perturbed systems and legacy codes. SIAM J. Appl. Dyn. Syst. **4**(3), 711–732 (2005). https://doi.org/10.1137/040608295
18. E. Bollt, Attractor modeling and empirical nonlinear model reduction of dissipative dynamical systems. International Journal of Bifurcation and Chaos **17**(04), 1199–1219 (2007). https://doi.org/10.1142/S021812740701777X
19. A. Quarteroni, G. Rozz, Reduced order methods for modeling and computational reduction, vol. 9 (Springer, Cham, 2014). https://doi.org/10.1007/978-3-319-02090-7
20. F. Regazzoni, L. Dede, A. Quarteroni, Machine learning for fast and reliable solution of time-dependent differential equations. J. Comput. Phys. **397**, 108852 (2019). https://doi.org/10.1016/j.jcp.2019.07.050
21. J.M. Ginoux, Slow invariant manifolds of slow-fast dynamical systems. International Journal of Bifurcation and Chaos **31**(07), 2150112 (2021). https://doi.org/10.1142/S0218127421501121
22. T.P. Sapsis, A. Blanchard, Optimal criteria and their asymptotic form for data selection in data-driven reduced-order modelling with Gaussian process regression. Phil. Trans. R. Soc. A **380**(2229), 20210197 (2022). https://doi.org/10.1098/rsta.2021.0197
23. D. Patsatzis, G. Fabiani, L. Russo, C. Siettos, Slow invariant manifolds of singularly perturbed systems via physics-informed machine learning. SIAM J. Sci. Comput. **46**(4), C297–C322 (2024). https://doi.org/10.1137/23M1602991
24. D.G. Patsatzis, L. Russo, C. Siettos, Slow invariant manifolds of fast-slow systems of ODEs with physics-informed neural networks. SIAM J. Appl. Dyn. Syst. **23**(4), 3077–3122 (2024). https://doi.org/10.1137/24M1656402
25. E.D. Koronaki, N. Evangelou, C.P. Martin-Linares, E.S. Titi, I.G. Kevrekidis, Nonlinear dimensionality reduction then and now: AIMs for dissipative PDEs in the ML era. J. Comput. Phys. **506**, 112910 (2024). https://doi.org/10.1016/j.jcp.2024.112910
26. R. Rico-Martinez, K. Krischer, I. Kevrekidis, M. Kube, J. Hudson, Discrete-vs. continuous-time nonlinear signal processing of Cu electrodissolution data. Chemical Engineering Communications **118**(1), 25–48 (1992). https://doi.org/10.1080/00986449208936084
27. R. González-García, R. Rico-Martìnez, I.G. Kevrekidis, Identification of distributed parameter systems: A neural net based approach. Computers & chemical engineering **22**, S965–S968 (1998). https://doi.org/10.1016/S0098-1354(98)00191-4
28. M. Raissi, P. Perdikaris, G.E. Karniadakis, Numerical Gaussian processes for time-dependent and nonlinear partial differential equations. SIAM J. Sci. Comput. **40**(1), A172–A198 (2018). https://doi.org/10.1137/17M1120762
29. P.R. Vlachas, W. Byeon, Z.Y. Wan, T.P. Sapsis, P. Koumoutsakos, Data-driven forecasting of high-dimensional chaotic systems with long short-term memory networks. Proceedings of the Royal Society A: Mathematical, Physical and Engineering Sciences **474**(2213), 20170844 (2018). https://doi.org/10.1098/rspa.2017.0844
30. S. Lee, M. Kooshkbaghi, K. Spiliotis, C.I. Siettos, I.G. Kevrekidis, Coarse-scale PDEs from fine-scale observations via machine learning. Chaos: An Interdisciplinary Journal of Nonlinear Science **30**(1) (2020). https://doi.org/10.1063/1.5126869
31. L. Lu, P. Jin, G. Pang, Z. Zhang, G.E. Karniadakis, Learning nonlinear operators via DeepONet based on the universal approximation theorem of operators. Nature machine intelligence **3**(3), 218–229 (2021). https://doi.org/10.1038/s42256-021-00302-5
32. E. Galaris, G. Fabiani, I. Gallos, I. Kevrekidis, C. Siettos, Numerical bifurcation analysis of PDEs from lattice Boltzmann model simulations: a parsimonious machine learning approach. J. Sci. Comput. **92**(2), 34 (2022). https://doi.org/10.1007/s10915-022-01883-y
33. D. Floryan, M.D. Graham, Data-driven discovery of intrinsic dynamics. Nature Machine Intelligence **4**(12), 1113–1120 (2022). https://doi.org/10.1038/s42256-022-00575-4
34. G. Fabiani, I.G. Kevrekidis, C. Siettos, A.N. Yannacopoulos, RandONets: Shallow networks with random projections for learning linear and nonlinear operators. J. Comput. Phys. **520**, 113433 (2025). https://doi.org/10.1016/j.jcp.2024.113433

35. C.I. Siettos, G.V. Bafas, A.G. Boudouvis, Truncated Chebyshev series approximation of fuzzy systems for control and nonlinear system identification. Fuzzy Sets Syst. **126**(1), 89–104 (2002). https://doi.org/10.1016/S0165-0114(01)00124-5
36. S.L. Brunton, J.L. Proctor, J.N. Kutz, Discovering governing equations from data by sparse identification of nonlinear dynamical systems. Proc. Natl. Acad. Sci. **113**(15), 3932–3937 (2016). https://doi.org/10.1073/pnas.1517384113
37. M. Raissi, P. Perdikaris, G.E. Karniadakis, Physics-informed neural networks: A deep learning framework for solving forward and inverse problems involving nonlinear partial differential equations. J. Comput. Phys. **378**, 686–707 (2019). https://doi.org/10.1016/j.jcp.2018.10.045
38. L. Yang, D. Zhang, G.E. Karniadakis, Physics-informed generative adversarial networks for stochastic differential equations. SIAM J. Sci. Comput. **42**(1), A292–A317 (2020). https://doi.org/10.1137/18M1225409
39. S. Lee, Y. Psarellis, C. Siettos, I.G. Kevrekidis, Learning black- and gray-box chemotactic PDEs/closures from agent based Monte Carlo simulation data. Journal of Mathematical Biology **87**(15) (2023). https://doi.org/10.1007/s00285-023-01946-0
40. G. Fabiani, N. Evangelou, T. Cui, J.M. Bello-Rivas, C.P. Martin-Linares, C. Siettos, I.G. Kevrekidis, Task-oriented machine learning surrogates for tipping points of agent-based models. Nat. Commun. **15**(1), 4117 (2024). https://doi.org/10.1038/s41467-024-48024-7
41. D.G. Patsatzis, M. di Bernardo, L. Russo, C. Siettos, GoRINNs: Godunov-riemann informed neural networks for learning hyperbolic conservation laws. J. Comput. Phys. **534**, 114002 (2025). https://doi.org/10.1016/j.jcp.2025.114002
42. K. Georgiou, C. Siettos, A.N. Yannacopoulos, Fredholm neural networks. SIAM J. Sci. Comput. **47**(4), C1006–C1031 (2025). https://doi.org/10.1137/24M1686991
43. G.C. Peng, M. Alber, A.B. Tepole, W.R. Cannon, S. De, S. Dura-Bernal, K. Garikipati, G. Karniadakis, W.W. Lytton, P. Perdikaris, L. Petzold, E. Kuhl, Multiscale modeling meets machine learning: What can we learn? Archives of computational methods in engineering: state of the art reviews **28**(3), 1017 (2020). https://doi.org/10.1007/s11831-020-09405-5
44. G.E. Karniadakis, I.G. Kevrekidis, L. Lu, P. Perdikaris, S. Wang, L. Yang, Physics-informed machine learning. Nature Reviews Physics **3**(6), 422–440 (2021). https://doi.org/10.1038/s42254-021-00314-5
45. J. Nathan Kutz, Machine Learning Methods for Constructing Dynamic Models From Data (Springer International Publishing), pp. 149–178 (2023). https://doi.org/10.1007/978-3-031-36644-4_4
46. C. Siettos, J. Starke, Multiscale modeling of brain dynamics: from single neurons and networks to mathematical tools. WIREs Syst. Biol. Med. **8**(5), 438–458 (2016). https://doi.org/10.1002/wsbm.1348
47. A. Anderson, M.S. Cohen, Decreased small-world functional network connectivity and clustering across resting state networks in schizophrenia: an fMRI classification tutorial. Front. Hum. Neurosci. **7**, 520 (2013). https://doi.org/10.3389/fnhum.2013.00520
48. I.K. Gallos, K. Gkiatis, G.K. Matsopoulos, C. Siettos, ISOMAP and machine learning algorithms for the construction of embedded functional connectivity networks of anatomically separated brain regions from resting state fMRI data of patients with schizophrenia. AIMS neuroscience **8**(2), 295 (2021). https://doi.org/10.3934/Neuroscience.2021016
49. D. Duncan, R. Talmon, H.P. Zaveri, R.R. Coifman, Identifying preseizure state in intracranial EEG data using diffusion kernels. Math. Biosci. Eng. **10**(3), 579–590 (2013). https://doi.org/10.3934/mbe.2013.10.579
50. W. Wu, S. Nagarajan, Z. Chen, Bayesian machine learning: EEG∨MEG signal processing measurements. IEEE Signal Process. Mag. **33**(1), 14–36 (2015). https://doi.org/10.1109/MSP.2015.2481559
51. J. Reidl, J. Starke, D.B. Omer, A. Grinvald, H. Spors, Independent component analysis of high-resolution imaging data identifies distinct functional domains. Neuroimage **34**(1), 94–108 (2007). https://doi.org/10.1016/j.neuroimage.2006.08.031
52. F.S. Kragelund, K. Spiliotis, M. Heerdegen, T. Sellmann, H. Bathel, A. Lüttig, A. Richter, J. Starke, R. Köhling, D. Franz, Network-wide effects of pallidal deep brain stimulation normalised abnormal cerebellar cortical activity in the dystonic animal model. Neurobiol. Dis. **205**, 106779 (2025). https://doi.org/10.1016/j.nbd.2024.106779
53. I.K. Gallos, E. Galaris, C.I. Siettos, Construction of embedded fMRI resting-state functional connectivity networks using manifold learning. Cogn. Neurodyn. **15**(4), 585–608 (2021). https://doi.org/10.1007/s11571-020-09645-y
54. I.K. Gallos, D. Lehmberg, F. Dietrich, C. Siettos, Data-driven modelling of brain activity using neural networks, diffusion maps, and the Koopman operator. Chaos: An Interdisciplinary Journal of Nonlinear Science **34**(1) (2024). https://doi.org/10.1063/5.0157881
55. T.N. Thiem, M. Kooshkbaghi, T. Bertalan, C.R. Laing, I.G. Kevrekidis, Emergent spaces for coupled oscillators. Front. Comput. Neurosci. **14**, 36 (2020). https://doi.org/10.3389/fncom.2020.00036
56. C.R. Laing, T. Frewen, I.G. Kevrekidis, Reduced models for binocular rivalry. J. Comput. Neurosci. **28**, 459–476 (2010). https://doi.org/10.1007/s10827-010-0227-6
57. M. Khosla, K. Jamison, A. Kuceyeski, M.R. Sabuncu, Ensemble learning with 3D convolutional neural networks for functional connectome-based prediction. Neuroimage **199**, 651–662 (2019). https://doi.org/10.1016/j.neuroimage.2019.06.012
58. E. Gleichgerrcht, B. Munsell, S. Bhatia, W.A. Vandergrift III., C. Rorden, C. McDonald, J. Edwards, R. Kuzniecky, L. Bonilha, Deep learning applied to whole-brain connectome to determine seizure control after epilepsy surgery. Epilepsia **59**(9), 1643–1654 (2018). https://doi.org/10.1111/epi.14528
59. F.P. Kemeth, T. Bertalan, T. Thiem, F. Dietrich, S.J. Moon, C.R. Laing, I.G. Kevrekidis, Learning emergent partial differential equations in a learned emergent space. Nat. Commun. **13**(1), 3318 (2022). https://doi.org/10.1038/s41467-022-30628-6

60. L.É. Lapicque, Recherches quantitatives sur l'excitation électrique des nerfs traitée comme une polarization. J. Physiol. Pathol. Gen. **9**, 620–635 (1907)
61. N. Fourcaud, N. Brunel, Dynamics of the firing probability of noisy integrate-and-fire neurons. Neural Comput. **14**(9), 2057–2110 (2002). https://doi.org/10.1162/089976602320264015
62. N. Brunel, M.C.W. van Rossum, Quantitative investigations of electrical nerve excitation treated as polarization. Biol. Cybern. **97**(5–6), 341 (2007). https://doi.org/10.1007/s00422-007-0189-6
63. I.G. Kevrekidis, C.W. Gear, J.M. Hyman, P.G. Kevrekidis, O. Runborg, C. Theodoropoulos, Equation-free, coarse-grained multiscale computation: enabling microscopic simulators to perform system-level analysis. Commun. Math. Sci. **1**(4), 715–762 (2003). https://doi.org/10.4310/cms.2003.v1.n4.a5
64. Y. Kevrekidis, G. Samaey, Equation-free modeling. Scholarpedia **5**(9), 4847 (2010). https://doi.org/10.4249/scholarpedia.4847. Revision #137023
65. C.R. Laing, On the application of "equation-free modelling" to neural systems. J. Comput. Neurosci. **20**(1), 5–23 (2006). https://doi.org/10.1007/s10827-006-3843-z
66. C.R. Laing, I.G. Kevrekidis, Equation-free analysis of spike-timing-dependent plasticity. Biol. Cybern. **109**, 701–714 (2015). https://doi.org/10.1007/s00422-015-0668-0
67. C. Marschler, C. Faust-Ellsässer, J. Starke, J.L. van Hemmen, Bifurcation of learning and structure formation in neuronal maps. Europhys. Lett. **108**(4), 48005 (2014). https://doi.org/10.1209/0295-5075/108/48005
68. K.G. Spiliotis, C.I. Siettos, A timestepper-based approach for the coarse-grained analysis of microscopic neuronal simulators on networks: Bifurcation and rare-events micro- to macro-computations. Neurocomputing **74**(17), 3576–3589 (2011). https://doi.org/10.1016/j.neucom.2011.06.018
69. C.E. Rasmussen, C.K.I. Williams, *Gaussian Processes for Machine Learning* (The MIT Press, Cambridge, MA, 2006). https://doi.org/10.7551/mitpress/3206.001.0001
70. C. Marschler, J. Sieber, R. Berkemer, A. Kawamoto, J. Starke, Implicit methods for equation-free analysis: Convergence results and analysis of emergent waves in microscopic traffic models. SIAM J. Appl. Dyn. Syst. **13**(3), 1202–1238 (2014). https://doi.org/10.1137/130913961
71. C. Marschler, J. Sieber, P.G. Hjorth, J. Starke, *Equation-Free Analysis of Macroscopic Behavior in Traffic and Pedestrian Flow*, in *Traffic and Granular Flow '13*, ed. by M. Chraibi, M. Boltes, A. Schadschneider, A. Seyfried (Springer International Publishing, Cham, 2015), pp. 423–439. https://doi.org/10.1007/978-3-319-10629-8_48
72. J. Sieber, C. Marschler, J. Starke, Convergence of equation-free methods in the case of finite time scale separation with application to deterministic and stochastic systems. SIAM J. Appl. Dyn. Syst. **17**(4), 2574–2614 (2018). https://doi.org/10.1137/17M1126084
73. D.G. Patsatzis, L. Russo, I.G. Kevrekidis, C. Siettos, Data-driven control of agent-based models: An equation/variable-free machine learning approach. J. Comput. Phys. **478**, 111953 (2023). https://doi.org/10.1016/j.jcp.2023.111953
74. F. Dietrich, A. Makeev, G. Kevrekidis, N. Evangelou, T. Bertalan, S. Reich, I.G. Kevrekidis, Learning effective stochastic differential equations from microscopic simulations: Linking stochastic numerics to deep learning. Chaos: An Interdisciplinary Journal of Nonlinear Science **33**(2) (2023). https://doi.org/10.1063/5.0113632
75. H.V. Alvarez, D.G. Patsatzis, L. Russo, I. Kevrekidis, C. Siettos, Next generation equation-free multiscale modelling of crowd dynamics via machine learning. arXiv preprint arXiv:2508.03926 (2025)
76. M. Heinonen, C. Yildiz, H. Mannerström, J. Intosalmi, H. Lähdesmäki, *Learning unknown ODE models with Gaussian processes*, in *Proceedings of the 35th International Conference on Machine Learning*, *Proceedings of Machine Learning Research*, vol. 80, ed. by J. Dy, A. Krause (PMLR, Stockholm, 2018), pp. 1959–1968
77. Y.M. Psarellis, T.P. Sapsis, I.G. Kevrekidis, Active search for bifurcations. Chaos: An Interdiscip. J. Nonlinear Sci. **35**(5), 053159 (2025). https://doi.org/10.1063/5.0226625
78. T. Chin, J. Ruth, C. Sanford, R. Santorella, P. Carter, B. Sandstede, Enabling equation-free modeling via diffusion maps. J. Dyn. Diff. Equat. **36**(Suppl 1), 415–434 (2024). https://doi.org/10.1007/s10884-021-10127-w
79. J. Wang, An intuitive tutorial to Gaussian process regression. Comput. Sci. & Eng. **25**(4), 4–11 (2023). https://doi.org/10.1109/MCSE.2023.3342149
80. C. Williams, C. Rasmussen, Gaussian Processes for Regression, in *Adv. Neural Inf. Processing Syst*, vol. 8, ed. by D. Touretzky, M. Mozer, M. Hasselmo (MIT Press, Cambridge, MA, 1995), pp.514–520
81. C.E. Rasmussen, *Gaussian Processes in Machine Learning* (Springer Berlin Heidelberg, 2004), pp. 63–71. https://doi.org/10.1007/978-3-540-28650-9_4
82. E. Schulz, M. Speekenbrink, A. Krause, A tutorial on Gaussian process regression: Modelling, exploring, and exploiting functions. J. Math. Psychol. **85**, 1–16 (2018). https://doi.org/10.1016/j.jmp.2018.03.001
83. N. Ulapane, K. Thiyagarajan, S. Kodagoda, *Hyper-parameter initialization for squared exponential kernel-based gaussian process regression*, in *2020 15th IEEE Conference on Industrial Electronics and applications (ICIEA)* (2020), pp. 1154–1159. https://doi.org/10.1109/ICIEA48937.2020.9248120
84. R.R. Coifman, S. Lafon, Diffusion maps. Appl. Comput. Harmon. Anal. **21**(1), 5–30 (2006). https://doi.org/10.1016/j.acha.2006.04.006
85. O.V. Popovych, P.A. Tass, Adaptive delivery of continuous and delayed feedback deep brain stimulation - a computational study. Sci. Rep. **9**(1), 10585 (2019). https://doi.org/10.1038/s41598-019-47036-4
86. G. Buzsáki, Large-scale recording of neuronal ensembles. Nat. Neurosci. **7**(5), 446–451 (2004). https://doi.org/10.1038/nn1233

87. D.J. Higham, An algorithmic introduction to numerical simulation of stochastic differential equations. SIAM Rev. **43**(3), 525–546 (2001). https://doi.org/10.1137/S0036144500378302
88. H. Wallner, T. Settmacher, K. Spiliotis, C. Siettos, J. Starke, Code and data used in this publication (2025). https://doi.org/10.5281/zenodo.17234700
89. J. Fairbrother, C. Nemeth, M. Rischard, J. Brea, T. Pinder, GaussianProcesses.jl: A Nonparametric Bayes Package for the Julia Language. Journal of Statistical Software **102**, 1–36 (2022). https://doi.org/10.18637/jss.v102.i01
90. P.K. Mogensen, A.N. Riseth, Optim: A mathematical optimization package for Julia. Journal of Open Source Software **3**(24), 615 (2018). https://doi.org/10.21105/joss.00615
91. D. Bachrathy, G. Stépán, Bisection method in higher dimensions and the efficiency number. Periodica Polytechnica. Engineering. Mechanical Engineering **56**(2), 81 (2012). https://doi.org/10.3311/pp.me.2012-2.01
92. E. Doedel, H.B. Keller, J.P. Kernevez, Numerical analysis and control of bifurcation problems (I): Bifurcation in finite dimensions. International Journal of Bifurcation and Chaos **01**(03), 493–520 (1991). https://doi.org/10.1142/S0218127491000397
93. K. Spiliotis, J. Starke, D. Franz, A. Richter, R. Köhling, Deep brain stimulation for movement disorder treatment: exploring frequency-dependent efficacy in a computational network model. Biol. Cybern. (2021). https://doi.org/10.1007/s00422-021-00909-2
94. K. Spiliotis, K. Butenko, J. Starke, U. van Rienen, R. Köhling, Towards an optimised deep brain stimulation using a large-scale computational network and realistic volume conductor model. J. Neural Eng. **20**(6), 066045 (2024). https://doi.org/10.1088/1741-2552/ad0e7c
95. S. Perl, A. Lüttig, R. Köhling, A. Richter, Deep brain stimulation in animal models of dystonia. Neurobiol. Dis. **175**, 105912 (2022). https://doi.org/10.1016/j.nbd.2022.105912
96. K. Spiliotis, R. Appali, A.K. Fontes Gomes, J.P. Payonk, S. Adrian, U. Van Rienen, J. Starke, R. Köhling, Utilising activity patterns of a complex biophysical network model to optimise intra-striatal deep brain stimulation. Scientific Reports **14**(1), 18919 (2024). https://doi.org/10.1038/s41598-024-69456-7
97. M.A. Álvarez, L. Rosasco, N.D. Lawrence, Kernels for vector-valued functions: A review. Found. Trends Mach. Learn. **4**(3), 195–266 (2012). https://doi.org/10.1561/2200000036